Appl. Math. Mech. -Engl. Ed., **41**(11), 1685–1696 (2020)

APPLIED MATHEMATICS AND MECHANICS (ENGLISH EDITION)

https://doi.org/10.1007/s10483-020-2680-8

Darcy-Forchheimer flow with nonlinear mixed convection*

T. HAYAT[1,2], F. HAIDER[1,†], A. ALSAEDI[2]

1. Department of Mathematics, Quaid-i-Azam University, Islamabad 44000, Pakistan;
2. Nonlinear Analysis and Applied Mathematics (NAAM) Research Group, Department of Mathematics, Faculty of Science, King Abdulaziz University, Jeddah 21589, Saudi Arabia

(Received May 14, 2020 / Revised Aug. 12, 2020)

Abstract An analysis of the mixed convective flow of viscous fluids induced by a nonlinear inclined stretching surface is addressed. Heat and mass transfer phenomena are analyzed with additional effects of heat generation/absorption and activation energy, respectively. The nonlinear Darcy-Forchheimer relation is deliberated. The dimensionless problem is obtained through appropriate transformations. Convergent series solutions are obtained by utilizing an optimal homotopic analysis method (OHAM). Graphs depicting the consequence of influential variables on physical quantities are presented. Enhancement in the velocity is observed through the local mixed convection parameter while an opposite trend of the concentration field is noted for the chemical reaction rate parameter.

Key words Darcy-Forchheimer porous space, nonlinear mixed convection, viscous fluid, heat generation/absorption, activation energy, optimal homotopic analysis method (OHAM)

Chinese Library Classification O357
2010 Mathematics Subject Classification 76S05

1 Introduction

The fluid flow through a porous space and objects of different shapes embedded in the porous space has recently attracted the attention of researchers. Its applications can be found in diversified disciplines such as nuclear engineering, bioengineering, mechanical engineering, geothermal physics, civil engineering, and applied mathematics. Geothermal energy utilization, solidification of casting, blood flow in lungs or in arteries, buried electrical cables, pollutants dispersion in aquifers, porous heat pipes, chemical catalytic connectors are some processes which involve the fluid flow through a porous space. Darcy's law is extensively used to interpret the flow filling the porous space. Darcy's law becomes invalid for effects of high velocity and turbulence in the porous space. The second-order polynomial function was introduced in the momentum equation by Forchheimer[1] to account for the effects of inertia on apparent permeability. Muskat[2] named it as the Forchheimer factor. Several studies

* Citation: HAYAT, T., HAIDER, F., and ALSAEDI, A. Darcy-Forchheimer flow with nonlinear mixed convection. *Applied Mathematics and Mechanics* (*English Edition*), **41**(11), 1685–1696 (2020) https://doi.org/10.1007/s10483-020-2680-8

† Corresponding author, E-mail: farwahaider@math.qau.edu.pk

considered the flow through a porous space by using the Darcy-Forchheimer relation in different geometries. Few of them are reported here. The Darcy-Forchheimer flow about an isothermal vertical flat plate with thermophoresis was analyzed by Seddeek[3]. Sadiq and Hayat[4] illustrated the Darcy-Forchheimer flow over a stretching surface. Bakar et al.[5] interpreted the Darcy-Forchheimer flow over a shrinking surface. Hayat et al.[6] extended the work by considering homogeneous-heterogeneous reactions and Cattaneo-Christov heat flux. The flow of nanofluids in a vertical rectangular duct was examined by Umavathi et al.[7]. They used the Darcy-Brinkman-Forchheimer relation for the flow through a porous space. Chakraborty et al.[8] discussed the Darcy-Forchheimer flow over an inclined porous plate. Seth et al.[9] provided the Darcy-Forchheimer flow over an inclined stretchable sheet. Soret and Dufour effects were also considered. The rotating flow of carbon nanotubes through a porous space was interpreted by Shah et al.[10]. Saif et al.[11] presented the flow of nanofluids through a porous space. The disturbance in the flow was generated by a curved stretching sheet. Rasool et al.[12] provided the Darcy-Forchheimer flow of nanofluids induced by a nonlinear stretching sheet. Sadiq et al.[13] analyzed the Darcy-Forchheimer flow over a rotating disk. Sheikholeslami et al.[14] presented the non-Darcy flow within the porous enclosure. A similar trend of the flow field was observed for the flow through a porous space in different geometries.

The mixed convective flow is prominent in various natural, engineering, and industrial processes. Applications of the mixed convective flow include different temperature atmospheric flows, lubrication grooves, lakes and reservoirs, and manufacturing of nuclear plants. For a thermal equipment which requires a high temperature to operate, the relation between temperature and concentration-dependent density becomes nonlinear. This nonlinear relation strongly affects the flow characteristics[15–21]. Heat and mass transfer over a moving surface can be prominent in manufacturing processes such as cooling towers, hot rolling, continuos casting, hot extrusion, crystal growth, and wire drawing. Vajravelu[22] provided numerical solutions for the flow over a nonlinear stretching surface. Thumma et al.[23] studied the flow of nanofluids induced by a nonlinear inclined stretching sheet. Magnetic field and heat generation/absorption were also considered. The chemically reactive flow of nanofluids induced by a porous stretchable sheet was analyzed by Jain et al.[24]. Gupta et al.[25] considered magnetohydrodynamic (MHD) and thermal radiation in the flow over an inclined stretchable sheet. Ghadikolaeia et al.[26] illustrated the nonlinear thermal radiation and Joule heating effects in the flow induced by an inclined stretching sheet. Gholinia et al.[27] presented the numerical investigation of the free convective flow induced by an inclined stretching sheet. Thriveni and Mahanthesh[28] analyzed heat transport of hybrid nanofluids in an annulus. Recent investigations on heat transfer in the presence of heat generation/absorption can be consulted in Refs. [29]–[33].

Activation energy is an amount of energy necessary for a chemical system with potential reactants to yield a chemical reaction. Activation energy is determined by the Arrhenius equation which describes the change in rate constants with temperature. A mass transfer phenomenon with chemical reaction is used in geothermal engineering, chemical engineering, mechano-chemistry, oil and water emulsions, and deterioration of materials. There is a complex relation between chemical reactions and mass transfer. This relation can be scrutinized for both fluid flow and mass transfer through fabrication and digestion of reactant species at different rates. Hsiao[34] provided the numerical analysis for manufacturing efficiency of a thermal extrusion system by utilizing an improved method of controlling parameters. Majeed et al.[35] analyzed the collective effects of binary chemical reaction and activation energy in the fluid flow with the second-order momentum slip condition. Khan et al.[36] discussed the effect of nonlinear thermal radiation along with activation energy. They observed an increase in concentration of species due to the higher activation energy parameter. Dhlamini et al.[37] extended the work by considering mixed convection. They noted an enhancement in concentration of chemical species by the use of heated plate. Irfan et al.[38] utilized nonlinear mixed convection for the flow of Carreau fluids. The concentration of species can be more enhanced by the nonlinear variation

of density than the linear variation.

In view of the aforementioned studies, it is analyzed that the combined impact of nonlinear mixed convection and activation energy past a nonlinear inclined stretching surface has not been studied yet. Fluids filling the porous space with the Darcy-Forchheimer expression are also considered. Heat transfer aspects are considered in presence of heat generation/absorption. Such investigation is useful in high-temperature polymeric mixtures, aerosol technique, and solar collector which operates at moderate to high temperatures. The nonlinear system of equations is obtained through suitable transformations. Analytical solutions are computed by the optimal homotopy analysis method (OHAM)[39–49]. Aspects of emerging parameters are physically illustrated. Graphs are portrayed for the effects of emerging parameters on physical quantities.

2 Model development

We consider the two-dimensional, incompressible, mixed convective flow of viscous fluids induced by a nonlinear stretching sheet. The surface is inclined at an acute angle ξ. Viscous fluids filling the porous media are specified by the Darcy-Forchheimer relation. Impacts of activation energy and heat generation/absorption are also considered. The Cartesian coordinate framework is adopted such that the surface is lined up in the x- and y-directions normal to the surface. Surface deforms continuously in the x-direction with a nonlinear velocity $U_{\rm w} = ax^n$ $(a > 0, n \geqslant 0)$. Using boundary-layer and Boussinesq approximation, the resulting problems are obtained as follows[16,38]:

$$\frac{\partial u}{\partial x} + \frac{\partial v}{\partial y} = 0, \tag{1}$$

$$u\frac{\partial u}{\partial x} + v\frac{\partial u}{\partial y} = \nu\frac{\partial^2 u}{\partial y^2} - \frac{\nu}{K}u - Fu^2 + g(\beta_0(T - T_\infty) + \beta_1(T - T_\infty)^2 + \beta_2(C - C_\infty) + \beta_3(C - C_\infty)^2)\cos\xi, \tag{2}$$

$$u\frac{\partial T}{\partial x} + v\frac{\partial T}{\partial y} = \alpha\frac{\partial^2 T}{\partial y^2} + \frac{Q_0}{(\rho c_p)}(T - T_\infty), \tag{3}$$

$$u\frac{\partial C}{\partial x} + v\frac{\partial C}{\partial y} = D\frac{\partial^2 C}{\partial y^2} - k_{\rm r}^2(C - C_\infty)\Big(\frac{T}{T_\infty}\Big)^m \exp\Big(\frac{-E^*}{k^*T}\Big), \tag{4}$$

$$\begin{cases} u = U_{\rm w}(x) = ax^n, \quad v = 0, \quad T = T_{\rm w}, \quad C = C_{\rm w} \quad \text{at} \quad y = 0, \\ u \to 0, \quad T \to T_\infty, \quad C \to C_\infty \quad \text{as} \quad y \to \infty. \end{cases} \tag{5}$$

Here, u and v depict the velocity components along the x- and y-directions, $F = \frac{C_{\rm b}^*}{K^{*1/2}}$ is the nonlinear inertia coefficient of the porous space, g is the gravity, $C_{\rm b}^*$ represents the drag coefficient, β_0, β_1, β_2, and β_3 are the first-order and second-order expansions of thermal and solutal coefficients, respectively, $k_{\rm r}$ is the chemical reaction constant, k^* is the Boltzmann constant, and E^* is the activation energy.

Select[20]

$$\begin{cases} u = ax^n f'(\zeta), \quad v = \sqrt{\dfrac{a\nu(n+1)}{2}}x^{\frac{n-1}{2}}\Big(f(\zeta) + \dfrac{n-1}{n+1}\zeta f'(\zeta)\Big), \\ \theta(\zeta) = \dfrac{T - T_\infty}{T_{\rm w} - T_\infty}, \quad \phi = \dfrac{C - C_\infty}{C_{\rm w} - C_\infty}, \quad \zeta = y\sqrt{\dfrac{a(n+1)}{2\nu}}x^{\frac{n-1}{2}}. \end{cases} \tag{6}$$

Then, Eq. (1) is identically justified, and Eqs. (2)–(5) yield

$$\Big(f''' - \frac{2}{n+1}\lambda f'\Big) + ff'' - \frac{2}{n+1}(n+F_{\rm r})\,f'^2 + \frac{2}{n+1}R_{\rm i}(\theta+\alpha_1\theta^2)\,\cos\xi$$
$$+ \frac{2}{n+1}R_{\rm i}N^*(\phi+\alpha_1\phi^2)\,\cos\xi = 0, \tag{7}$$
$$\frac{1}{Pr}\theta'' + \frac{2}{n+1}\delta\theta + f\theta' = 0, \tag{8}$$
$$\frac{1}{Sc}\phi'' + f\phi' - \frac{2}{n+1}\Lambda(1+\Lambda^*\theta)^m \exp\Big(\frac{-E}{1+\Lambda^*\theta}\Big)\,\phi = 0, \tag{9}$$
$$\begin{cases} f=0, \quad f'=1, \quad \theta=1, \quad \phi=1 \quad \text{at} \quad \zeta=0, \\ f'\to 0, \quad \theta\to 0, \quad \phi\to 0 \quad \text{as} \quad \zeta\to\infty. \end{cases} \tag{10}$$

In the above expressions, λ depicts the local porosity parameter, $R_{\rm i}$ is the local mixed convection parameter, $F_{\rm r}$ is the Forchheimer number, α_1 is the nonlinear density-temperature parameter, α_2 is the nonlinear density-concentration parameter, N^* is the Buoyancy ratio parameter, δ is the local heat generation/absorption coefficient, Pr is the Prandtl number, Λ^* is the temperature difference variable, E is the activation energy parameter, Λ is the local reaction rate parameter, and Sc represents the Schmidt number. Here, one has

$$\begin{cases} \lambda = \dfrac{\nu}{Kax^{n-1}}, \quad F_{\rm r} = \dfrac{C_{\rm b}}{K^{1/2}}, \quad R_{\rm i} = \dfrac{g\beta_0(T_{\rm w}-T_\infty)}{a^2x^{2n-1}}, \quad \alpha_1 = \dfrac{\beta_1(T_{\rm w}-T_\infty)}{\beta_0}, \\ \alpha_2 = \dfrac{\beta_3(C_{\rm w}-C_\infty)}{\beta_2}, \quad N^* = \dfrac{\beta_2(C_{\rm w}-C_\infty)}{\beta_0(T_{\rm w}-T_\infty)}, \quad \delta = \dfrac{Q_0}{(\rho c_p)\,ax^{n-1}}, \quad Pr = \dfrac{\nu}{\alpha}, \\ E = \dfrac{E^*}{k^*T_\infty}, \quad \Lambda^* = \dfrac{T_{\rm w}-T_\infty}{T_\infty}, \quad \Lambda = \dfrac{k_{\rm r}^2}{ax^{n-1}}, \quad Sc = \dfrac{\nu}{D}. \end{cases} \tag{11}$$

The skin friction coefficient and local heat and mass transfer rates are

$$\begin{cases} C_{fx}Re_x^{1/2} = \Big(\dfrac{n+1}{2}\Big)^{1/2} f''(0), \\ Nu_xRe_x^{-1/2} = -\Big(\dfrac{n+1}{2}\Big)^{1/2}\theta'(0), \\ Sh_xRe_x^{-1/2} = -\Big(\dfrac{n+1}{2}\Big)^{1/2}\phi'(0), \end{cases} \tag{12}$$

in which $Re_x = \frac{ax^{n+1}}{\nu}$ is the local Reynolds number.

3 Solutions by the OHAM

Auxiliary linear operators and appropriate initial deformations for OHAM solutions are

$$L_f = \frac{{\rm d}^3}{{\rm d}\zeta^3} - \frac{\rm d}{{\rm d}\zeta}, \quad L_\theta = \frac{{\rm d}^2}{{\rm d}\zeta^2} - 1, \quad L_\phi = \frac{{\rm d}^2}{{\rm d}\zeta^2} - 1, \tag{13}$$
$$f_0(\zeta) = 1 - {\rm e}^{-\zeta}, \quad \theta_0(\zeta) = {\rm e}^{-\zeta}, \quad \phi_0(\zeta) = {\rm e}^{-\zeta} \tag{14}$$

with characteristics

$$\begin{cases} L_f(\widetilde{J}_1^{***} + \widetilde{J}_2^{***}{\rm e}^{\zeta} + \widetilde{J}_3^{***}{\rm e}^{-\zeta}) = 0, \quad L_\theta(\widetilde{J}_4^{***} + \widetilde{J}_5^{***}{\rm e}^{\zeta}) = 0, \\ L_\phi(\widetilde{J}_6^{***}{\rm e}^{\zeta} + \widetilde{J}_7^{***}{\rm e}^{-\zeta}) = 0. \end{cases} \tag{15}$$

Here, $\widetilde{J}_j^{***}$ $(j = 1, 2, \cdots, 7)$ represent arbitrary constants.

4 Solution convergence

The solution expressions consist of $\widehat{\hbar}_f$, $\widehat{\hbar}_\theta$, and $\widehat{\hbar}_\phi$ which play an essential role in convergent series solutions. The concept of minimization is utilized for obtaining optimal data of $\widehat{\hbar}_f$, $\widehat{\hbar}_\theta$, and $\widehat{\hbar}_\phi$. The average squared residual errors as recommended by Liao[39] are given as

$$\varepsilon_m^f = \frac{1}{k+1}\sum_{i=0}^{k}\Big(N_f\Big(\sum_{j=0}^{m}\widehat{f}(\zeta),\sum_{j=0}^{m}\widehat{\theta}(\zeta),\sum_{j=0}^{m}\widehat{\phi}(\zeta)\Big)_{\zeta=i\delta\zeta}\Big)^2, \tag{16}$$

$$\varepsilon_m^\theta = \frac{1}{k+1}\sum_{i=0}^{k}\Big(N_\theta(\sum_{j=0}^{m}\widehat{f}(\zeta),\sum_{j=0}^{m}\widehat{\theta}(\zeta))_{\zeta=i\delta\zeta}\Big)^2, \tag{17}$$

$$\varepsilon_m^\phi = \frac{1}{k+1}\sum_{i=0}^{k}\Big(N_\phi(\sum_{j=0}^{m}\widehat{f}(\zeta),\sum_{j=0}^{m}\widehat{\theta}(\zeta),\sum_{j=0}^{m}\widehat{\phi}(\zeta))_{\zeta=i\delta\zeta}\Big)^2, \tag{18}$$

$$\varepsilon_m^{\mathrm{t}} = \varepsilon_m^f + \varepsilon_m^\theta + \varepsilon_m^\phi, \tag{19}$$

where $\varepsilon_m^{\mathrm{t}}$ depicts the total squared residual error, $\delta\zeta = 0.5$, and $k = 20$. The optimal data of convergence control variables for $n = 0.5$ and $n = 1.5$ yield $\widehat{\hbar}_f = -1.350\,58$, $\widehat{\hbar}_\theta = -1.377\,47$, $\widehat{\hbar}_\phi = -1.313\,62$ and $\widehat{\hbar}_f = -0.701\,359$, $\widehat{\hbar}_\theta = -1.371\,73$, $\widehat{\hbar}_\phi = -1.338\,06$, while the total averaged squared residual errors for $n = 0.5$ and $n = 1.5$ are $\varepsilon_m^{\mathrm{t}} = 3.89 \times 10^{-3}$ and $\varepsilon_m^{\mathrm{t}} = 3.59 \times 10^{-3}$, respectively. Plots for the total residual error for $n = 0.5$ and $n = 1.5$ are portrayed in Figs. 1 and 2. Tables 1 and 2 are arranged for numerical values of the individual average squared residual error at $n = 0.5$ and $n = 1.5$, respectively. A decreasing trend of the average squared residual error is noted for higher-order deformations.

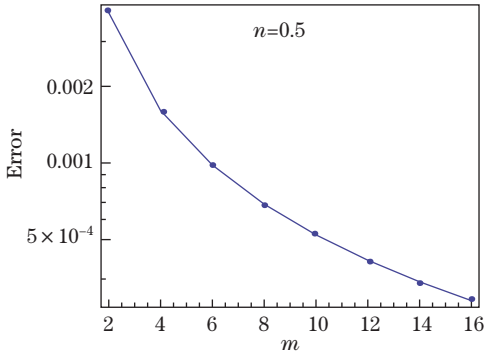

Fig. 1 Total residual error when $n = 0.5$

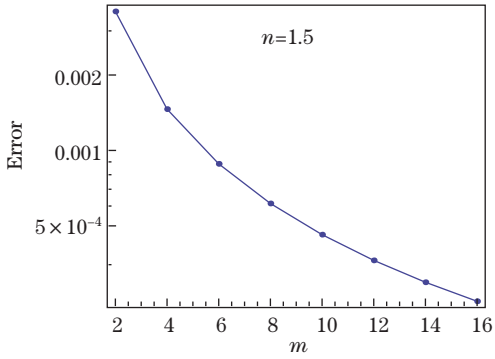

Fig. 2 Total residual error when $n = 1.5$

Table 1 Individual averaged squared residual errors when $n = 0.5$[6]

m	ε_m^f	ε_m^θ	ε_m^ϕ
2	1.05×10^{-4}	3.38×10^{-3}	4.04×10^{-4}
6	3.20×10^{-5}	9.14×10^{-4}	3.54×10^{-5}
10	1.93×10^{-5}	4.93×10^{-4}	9.57×10^{-6}
14	1.36×10^{-5}	3.23×10^{-4}	3.81×10^{-6}
16	1.18×10^{-5}	2.73×10^{-4}	2.63×10^{-6}

Table 2 Individual averaged squared residual errors when $n = 1.5$[6]

m	ε_m^f	ε_m^θ	ε_m^ϕ
2	1.34×10^{-4}	2.72×10^{-3}	8.55×10^{-4}
6	2.48×10^{-5}	7.20×10^{-4}	1.40×10^{-4}
10	2.03×10^{-5}	3.84×10^{-4}	5.63×10^{-5}
14	1.79×10^{-5}	3.06×10^{-4}	4.02×10^{-5}
16	1.43×10^{-5}	2.12×10^{-4}	2.34×10^{-5}

5 Discussion

This section intends to inspect the contribution of the local porosity parameter λ, the local Forchheimer number $F_{\rm r}$, the local mixed convection parameter $R_{\rm i}$, the nonlinear density-temperature parameter α_1, the nonlinear density-concentration parameter α_2, the inclination angle ξ, the Buoyancy ratio parameter N^*, the local heat generation/absorption coefficient δ, the Prandtl number Pr, the activation energy parameter E, the temperature difference parameter Λ^*, the local reaction rate parameter Λ, and the Schmidt number Sc on the velocity $f'(\zeta)$, thermal $\theta(\zeta)$ and concentration $\phi(\zeta)$ fields. The computations have been done for distinct values of $0 \leqslant \lambda \leqslant 1.2, 0 \leqslant F_{\rm r} \leqslant 1.4, 0 \leqslant R_{\rm i} \leqslant 0.9, 0 \leqslant \alpha_1 \leqslant 12, 0 \leqslant \alpha_2 \leqslant 12$, $0 \leqslant \xi \leqslant \frac{\pi}{2}, 0 \leqslant N^* \leqslant 2.0, -0.3 \leqslant \delta \leqslant 0.3, 0.7 \leqslant Pr \leqslant 1.4, 0 \leqslant E \leqslant 3, 1 \leqslant \Lambda^* \leqslant 4, 0 \leqslant m \leqslant 3$, $0 \leqslant \Lambda \leqslant 1.5$, and $0.5 \leqslant Sc \leqslant 1.5$[6,38]. The curves of $f'(\zeta)$ for λ estimations are deliberated in Fig. 3. Here, $f'(\zeta)$ lowers for higher λ. Physically, the presence of the porous space creates resistance in the smooth movement of fluid particles, which consequently declines the velocity field. Figure 4 portrays the significant impact of $F_{\rm r}$ on $f'(\zeta)$. Reduction in $f'(\zeta)$ is noticed for larger $F_{\rm r}$. Figure 5 shows the salient features of $R_{\rm i}$ on $f'(\zeta)$. Higher estimation of $R_{\rm i}$ predicts a strong buoyancy force within the fluid flow which intensifies the velocity for both $n = 0.5$ and $n = 1.5$. The variation of $f'(\zeta)$ via α_1 and α_2 is pointed out in Figs. 6 and 7, respectively. Clearly, $f'(\zeta)$ enhances for increasing values of α_1 and α_2. They signify the relative impact of thermal and solutal buoyancy forces on viscous hydrodynamic forces, respectively. Thus, the velocity increases due to the enhancement of buoyancy forces[28]. Figure 8 is analyzed for the role of N^* on $f'(\zeta)$. An enhancement in $f'(\zeta)$ is observed for larger N^* for both $n = 0.5$ and $n = 1.5$. $N^* > 1$ corresponds to the situation when solutal buoyancy forces exceed thermal buoyancy forces, $N^* < 1$ when solutal buoyancy forces are less than thermal buoyancy forces, and $N^* = 1$ when both the buoyancy forces are of the same magnitudes. Figure 9 presents the consequences of ξ on $f'(\zeta)$. It describes that $f'(\zeta)$ reduces for higher ξ. Attributes of δ against $\theta(\zeta)$ are declared in Fig. 10. It is investigated that an enhancement in δ yields stronger $\theta(\zeta)$ and a larger related layer thickness for both $n = 0.5$ and $n = 1.5$. It is due to the increase in buoyancy forces for heat generation which influences the flow rate. This enhancement in the flow rate causes stronger $\theta(\zeta)$. $\theta(\zeta)$ against Pr is sketched in Fig. 11. Pr possesses a converse relation with the thermal diffusivity. The less thermal diffusivity is noted for higher Pr which reduces the fluid temperature. Aspects of E on $\phi(\zeta)$ are displayed in Fig. 12. An increment in E gives rise to stronger $\phi(\zeta)$ and a larger associated layer thickness. Physically, higher E represents the decrease in the modified Arrhenius function which pushes the generative chemical reaction. The impact of Λ^* on $\phi(\zeta)$ is plotted in Fig. 13. Larger Λ^* indicates the decrease in $\phi(\zeta)$ and the related layer thickness for both $n = 0.5$ and $n = 1.5$. From Fig. 14, it is recognized that larger m produces weaker $\phi(\zeta)$ and a smaller associated layer thickness. Figure 15 is sketched to examine the variation in $\phi(\zeta)$ for Λ. An increase in Λ leads to the destructive chemical reaction that dissolves the liquid species more effectively which causes weaker $\phi(\zeta)$. The role of Sc on $\phi(\zeta)$ is pointed out in Fig. 16. Clearly, both $\phi(\zeta)$ and the corresponding layer thickness are reduced for higher Sc. Figures 17 and 18 characterize the consequences of α_1, α_2, and ξ on the skin friction coefficient $C_{fx}Re_x^{1/2}$. It is analyzed that $C_{fx}Re_x^{1/2}$ is lower when the increasing values of α_1, α_2,

and ξ are accounted. By increasing Pr and α, the magnitude of $Nu_x Re_x^{-1/2}$ is reduced for both $n = 0.5$ and $n = 1.5$ (see Figs. 19 and 20). Figures 21 and 22 address the local Sherwood number $Sh_x Re_x^{-1/2}$ for Λ, Λ^*, and m. Clearly, the magnitude of $Sh_x Re_x^{-1/2}$ is increased for higher estimations of Λ, Λ^*, and m. Tables 3 and 4 are arranged for the justification of the current results which are compared with those by Vajravelu and Sastri[15]. It is analyzed that the current results are in good agreement with those in Ref. [15].

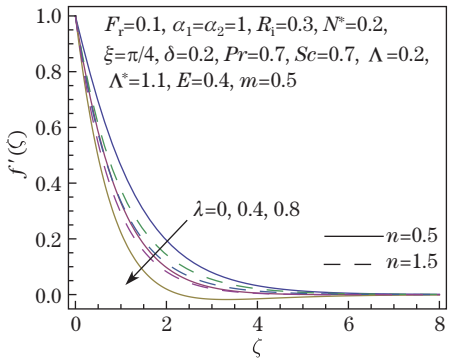

Fig. 3 Variation of $f'(\zeta)$ against λ (color online)

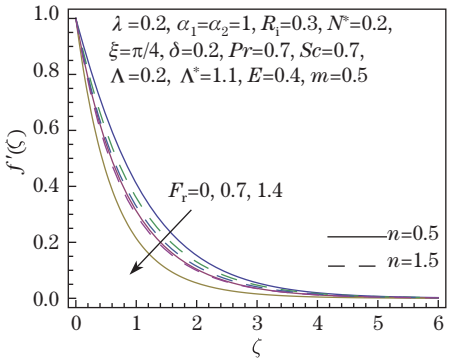

Fig. 4 Variation of $f'(\zeta)$ against F_r (color online)

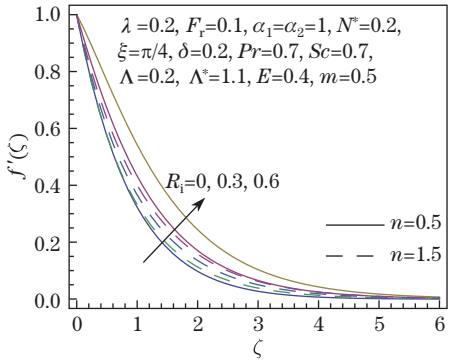

Fig. 5 Variation of $f'(\zeta)$ against R_i (color online)

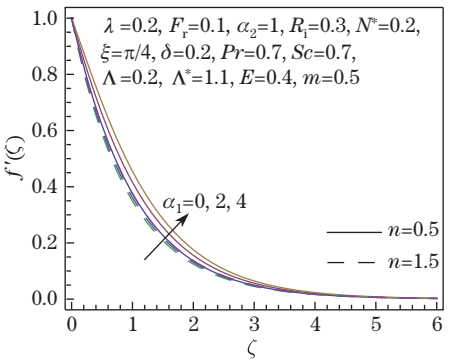

Fig. 6 Variation of $f'(\zeta)$ against α_1 (color online)

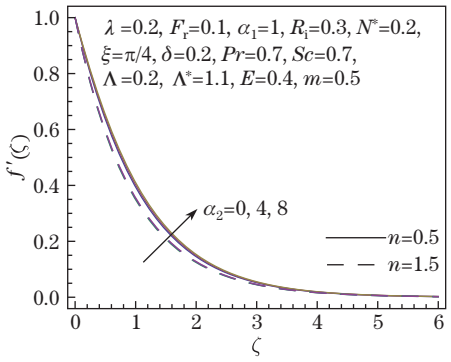

Fig. 7 Variation of $f'(\zeta)$ against α_2 (color online)

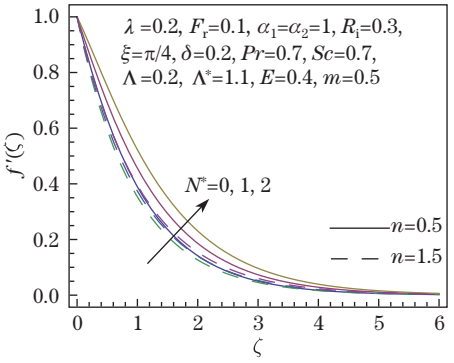

Fig. 8 Variation of $f'(\zeta)$ against N^* (color online)

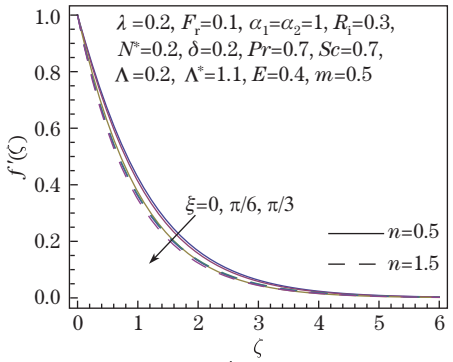

Fig. 9 Variation of $f'(\zeta)$ against ξ (color online)

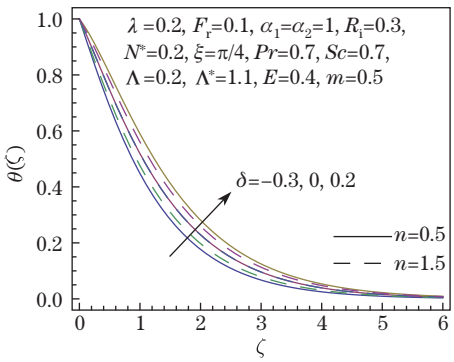

Fig. 10 Variation of $\theta(\zeta)$ against δ (color online)

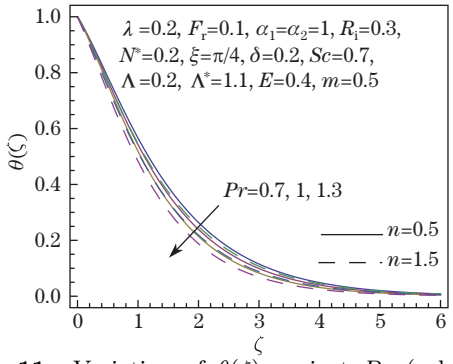

Fig. 11 Variation of $\theta(\zeta)$ against Pr (color online)

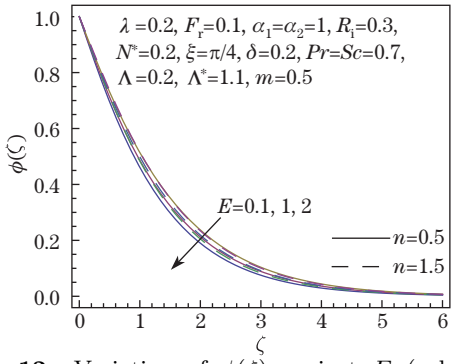

Fig. 12 Variation of $\phi(\zeta)$ against E (color online)

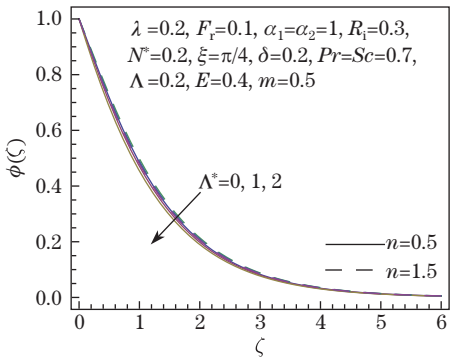

Fig. 13 Variation of $\phi(\zeta)$ against Λ^* (color online)

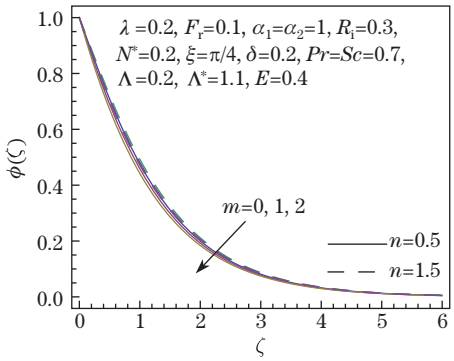

Fig. 14 Variation of $\phi(\zeta)$ against m (color online)

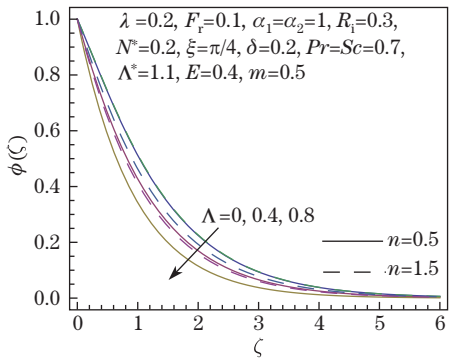

Fig. 15 Variation of $\phi(\zeta)$ against Λ (color online)

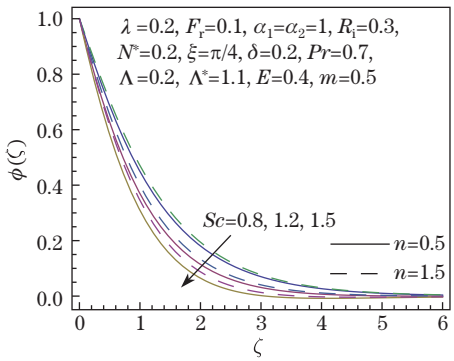

Fig. 16 Variation of $\phi(\zeta)$ against Sc (color online)

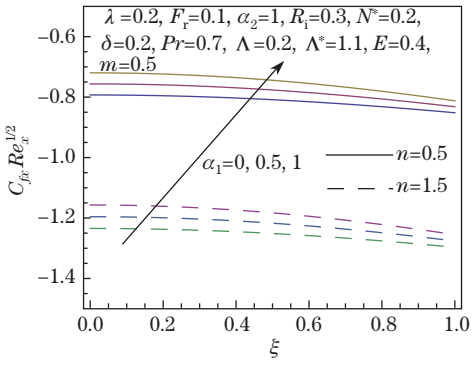

Fig. 17 Variation of $C_{fx}Re_x^{1/2}$ against α_1 and ξ (color online)

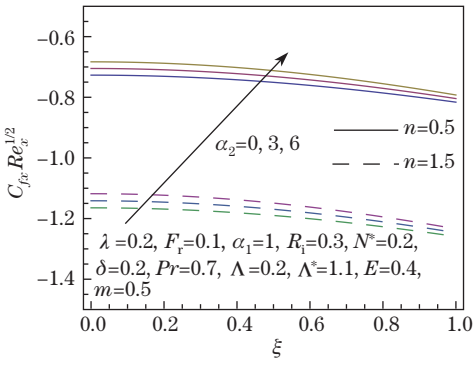

Fig. 18 Variation of $C_{fx}Re_x^{1/2}$ against α_2 and ξ (color online)

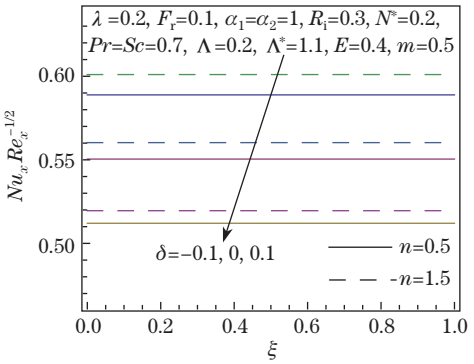

Fig. 19 Variation of $Nu_xRe_x^{-1/2}$ against δ and ξ (color online)

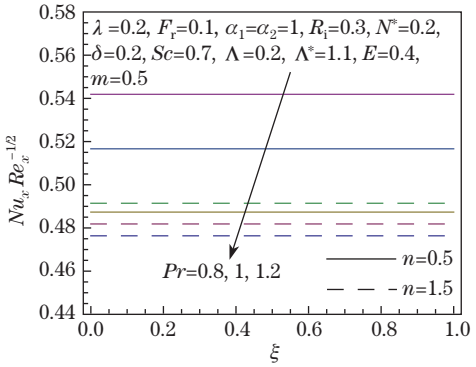

Fig. 20 Variation of $Nu_xRe_x^{-1/2}$ against Pr and ξ (color online)

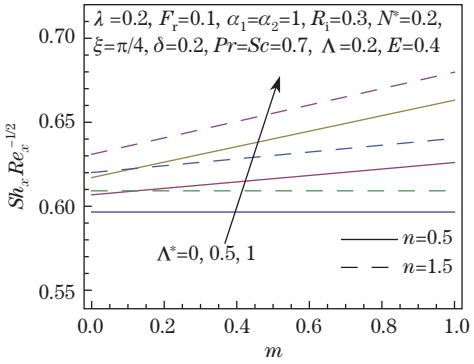

Fig. 21 Variation of $Sh_xRe_x^{-1/2}$ against Λ^* and m (color online)

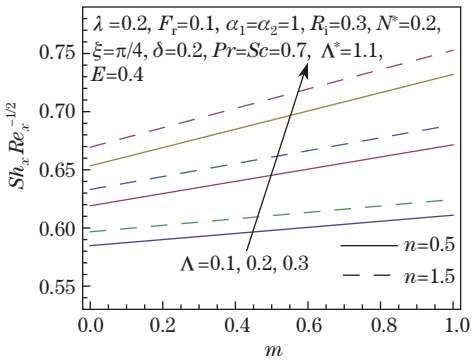

Fig. 22 Variation of $Sh_xRe_x^{-1/2}$ against Λ and m (color online)

Table 3 Comparative values of $-f''(0)$ for distinct values of n when $R_i = \alpha_1 = \alpha_2 = N^* = \lambda = F_r = 0$

n	$-f''(0)$	
	Present	Ref. [15]
1	1.000 0	1.000 0
5	1.194 5	1.194 5
10	1.234 9	1.234 8

Table 4 Comparative values of $-\theta'(0)$ for distinct values of n when $\delta = 0$

n	Pr	$-\theta'(0)$	
		Present	Ref. [15]
1	0.71	0.458 6	0.459 0
5		0.439 2	0.439 4
10		0.435 7	0.435 7
1	7.0	1.888 1	1.895 3
5		1.856 1	1.861 0
10		1.845 5	1.854 1

6 Conclusions

The nonlinear mixed convective flow by a nonlinear inclined stretching surface with the activation energy and the Darcy-Forchheimer porous space is modeled. Heat generation/ absorption is also considered. The key findings of the present analysis are outlined as follows.

(i) The velocity is an increasing function of R_{i}.

(ii) The improvement in the velocity is observed through α_1 and α_2.

(iii) The opposite trend of the velocity is noticed for N^* and ξ.

(iv) The stronger temperature is noted for larger δ.

(v) The concentration for Λ and Λ^* has a similar trend.

(vi) The concentration against E is enhanced.

(vii) The skin friction coefficient reduces for α_1 and α_2.

(viii) The variation of ξ results in augmentation of the local Nusselt number.

References

[1] FORCHHEIMER, P. Wasserbewegung durch boden. *Zeitschrift des Vereins Deutscher Ingenieure*, **45**, 1782–1788 (1901)

[2] MUSKAT, M. *The Flow of Homogeneous Fluids Through Porous Media*, McGraw-Hill, New York (1946)

[3] SEDDEEK, M. A. Influence of viscous dissipation and thermophoresis on Darcy-Forchheimer mixed convection in a fluid saturated porous media. *Journal of Colloid and Interface Science*, **293**, 137–142 (2006)

[4] SADIQ, M. A. and HAYAT, T. Darcy-Forchheimer flow of magneto Maxwell liquid bounded by convectively heated sheet. *Results in Physics*, **6**, 884–890 (2016)

[5] BAKAR, S. A., ARIFIN, N. M., NAZAR, R., ALI, F. M., and POP, I. Forced convection boundary layer stagnation-point flow in Darcy-Forchheimer porous medium past a shrinking sheet. *Frontiers in Heat and Mass Transfer*, **7**, 38 (2016)

[6] HAYAT, T., HAIDER, F., MUHAMMAD, T., and ALSAEDI, A. Darcy-Forchheimer flow with Cattaneo-Christov heat flux and homogeneous-heterogeneous reactions. *PLoS One*, **12**, e0174938 (2017)

[7] UMAVATHI, J. C., OJJELA, O., and VAJRAVELU, K. Numerical analysis of natural convective flow and heat transfer of nanofluids in a vertical rectangular duct using Darcy-Forchheimer-Brinkman model. *International Journal of Thermal Sciences*, **111**, 511–524 (2017)

[8] CHAKRABORTY, T., DAS, K., and KUNDU, P. K. Ag-water nanofluid flow over an inclined porous plate embedded in a non-Darcy porous medium due to solar radiation. *Journal of Mechanical Science and Technology*, **31**, 2443–2449 (2017)

[9] SETH, G., TRIPATHI, R., and RASHIDI, M. M. Hydromagnetic natural convection flow in a non-Darcy medium with Soret and Dufour effects past an inclined stretching sheet. *Journal of Porous Media*, **20**, 941–960 (2017)

[10] SHAH, Z., DAWAR, A., ISLAM, S., KHAN, I., and CHING, D. L. C. Darcy-Forchheimer flow of radiative carbon nanotubes with microstructure and inertial characteristics in the rotating frame. *Case Studies in Thermal Engineering*, **12**, 823–832 (2018)

[11] SAIF, R. S., HAYAT, T., ELLAHI, R., MUHAMMAD, T., and ALSAEDI, A. Darcy-Forchheimer flow of nanofluid due to a curved stretching surface. *International Journal of Numerical Methods for Heat and Fluid Flow*, **29**, 2–20 (2019)

[12] RASOOL, G., SHAFIQ, A., KHALIQUE, C. M., and ZHANG, T. Magnetohydrodynamic Darcy-Forchheimer nanofluid flow over a nonlinear stretching sheet. *Physica Scripta*, **94**, 105221 (2019)

[13] SADIQ, M. A., HAIDER, F., HAYAT, T., and ALSAEDI, A. Partial slip in Darcy-Forchheimer carbon nanotubes flow by rotating disk. *International Communications in Heat and Mass Transfer*, **116**, 104641 (2020)

[14] SHEIKHOLESLAMI, M., ARABKOOHSAR, A., and ISMAIL, K. A. R. Entropy analysis for a nanofluid within a porous media with magnetic force impact using non-Darcy model. *International Communications in Heat and Mass Transfer*, **112**, 104488 (2020)

[15] VAJRAVELU, K. and SASTRI, K. S. Fully developed laminar free convection flow between two parallel vertical walls-I. *International Journal of Heat and Mass Transfer*, **20**, 655–660 (1977)

[16] PARTHA, M. K. Nonlinear convection in a non-Darcy porous medium. *Applied Mathematics and Mechanics* (*English Edition*), **31**, 565–574 (2010) https://doi.org/10.1007/s10483-010-0504-6

[17] KAMESWARAN, P. K., SIBANDA, P., PARTHA, M. K., and MURTHY, P. V. S. N. Thermophoretic and nonlinear convection in non-Darcy porous medium. *Journal of Heat Transfer*, **136**, 042601–042609 (2014)

[18] SHEIKHOLESLAMI, M., HAYAT, T., and ALSAEDI, A. On simulation of nanofluid radiation and natural convection in an enclosure with elliptical cylinders. *International Journal of Heat and Mass Transfer*, **115**, 981–991 (2017)

[19] SRINIVASACHARYA, D., RAMREDDY, C., and NAVEEN, P. Double dispersion effect on nonlinear convective flow over an inclined plate in a micropolar fluid saturated non-Darcy porous medium. *Engineering Science and Technology, an International Journal*, **21**, 984–995 (2018)

[20] PATIL, P. M., SHASHIKANT, A., and HIREMATH, P. S. Diffusion of liquid hydrogen and oxygen in nonlinear mixed convection nanofluid flow over vertical cone. *International Journal of Hydrogen Energy*, **44**, 17061–17071 (2019)

[21] KHAN, M. I., ALZAHRANI, F., and HOBINY, A. Heat transport and nonlinear mixed convective nanomaterial slip flow of Walter-B fluid containing gyrotactic microorganisms. *Alexandria Engineering Journal*, **59**, 1761–1769 (2020)

[22] VAJRAVELU, K. Viscous flow over nonlinearly stretching sheet. *Applied Mathematics and Computation*, **124**, 281–288 (2001)

[23] THUMMA, T., BÉG, O. A., and KADIR, A. Numerical study of heat source/sink effects on dissipative magnetic nanofluid flow from a non-linear inclined stretching/shrinking sheet. *Journal of Molecular Liquids*, **232**, 159–173 (2017)

[24] JAIN, S., KUMARI, M., and PARMAR, A. Unsteady MHD chemically reacting mixed convection nano-fluids flow past an inclined porous stretching sheet with slip effect and variable thermal radiation and heat source. *Materials Today: Proceedings*, **5**, 6297–6312 (2018)

[25] GUPTA, S., KUMAR, D., and SINGH, J. MHD mixed convective stagnation point flow and heat transfer of an incompressible nanofluid over an inclined stretching sheet with chemical reaction and radiation. *International Journal of Heat and Mass Transfer*, **118**, 378–387 (2018)

[26] GHADIKOLAEIA, S. S., HOSSEINZADEH, K., GANJI, D. D., and JAFARI, B. Nonlinear thermal radiation effect on magneto Casson nanofluid flow with Joule heating effect over an inclined porous stretching sheet. *Case Studies in Thermal Engineering*, **12**, 176–187 (2018)

[27] GHOLINIA, M., HOSEINI, M. E., and GHOLINIA, S. A numerical investigation of free convection MHD flow of Walters-B nanofluid over an inclined stretching sheet under the impact of Joule heating. *Thermal Science and Engineering Progress*, **11**, 272–282 (2019)

[28] THRIVENI, K. and MAHANTHESH, B. Optimization and sensitivity analysis of heat transport of hybrid nanoliquid in an annulus with quadratic Boussinesq approximation and quadratic thermal radiation. *European Physical Journal Plus*, **135**, 459 (2020)

[29] MAHANTHESH, B., GIREESHA, B. J., and GORLA, R. S. R. Heat and mass transfer effects on the mixed convective flow of chemically reacting nanofluid past a moving/stationary vertical plate. *Alexandria Engineering Journal*, **55**, 569–581 (2016)

[30] SHEIKHOLESLAMI, M., KATARIA, H. R., and MITTAL, A. S. Effect of thermal diffusion and heat-generation on MHD nanofluid flow past an oscillating vertical plate through porous medium. *Journal of Molecular Liquids*, **2571**, 12–25 (2018)

[31] MAHAMTHESH, B., ANIMASAUN, I. L., RAHIMI-GORJI, M., and ALARIFI, I. M. Quadratic convective transport of dusty Casson and dusty Carreau fluids past a stretched surface with nonlinear thermal radiation, convective condition and non-uniform heat source/sink. *Physica A*, **535**, 122471 (2019)

[32] ALI, U., MALIK, M. Y., ALDERREMY, A. A., ALY, S., and REHMAN, K. U. A generalized findings on thermal radiation and heat generation/absorption in nanofluid flow regime. *Physica A*, **553**, 124026 (2020)

[33] MITTAL, A. S. and PATEL, H. R. Influence of thermophoresis and Brownian motion on mixed convection two dimensional MHD Casson fluid flow with non-linear radiation and heat generation. *Physica A*, **537**, 122710 (2020)

[34] HSIAO, K. L. To promote radiation electrical MHD activation energy thermal extrusion manufacturing system efficiency by using Carreau-nanofluid with parameters control method. *Energy*, **130**, 486–499 (2017)

[35] MAJEED, A., NOORI, F. M., ZEESHAN, A., MAHMOOD, T., REHMAN, S. U., and KHAN, I. Analysis of activation energy in magnetohydrodynamic flow with chemical reaction and second order momentum slip model. *Case Studies in Thermal Engineering*, **12**, 765–773 (2018)

[36] KHAN, M. I., HAYAT, T., KHAN, M. I., and ALSAEDI, A. Activation energy impact in nonlinear radiative stagnation point flow of Cross nanofluid. *International Communications in Heat and Mass Transfer*, **91**, 216–224 (2018)

[37] DHLAMINI, M., KAMESWARAN, P. K., SIBANDA, P., MOTSA, S., and MONDAL, H. Activation energy and binary chemical reaction effects in mixed convective nanofluid flow with convective boundary conditions. *Journal of Computational Design and Engineering*, **6**, 149–158 (2019)

[38] IRFAN, M., KHAN, W. A., KHAN, M., and GULZAR, M. M. Influence of Arrhenius activation energy in chemically reactive radiative flow of 3D Carreau nanofluid with nonlinear mixed convection. *Journal of Physics and Chemistry of Solids*, **125**, 141–152 (2019)

[39] LIAO, S. J. An optimal homotopy-analysis approach for strongly nonlinear differential equations. *Communications in Nonlinear Science and Numerical Simulation*, **15**, 2003–2016 (2010)

[40] MALVANDI, A., HEDAYATI, F., and DOMAIRRY, G. Stagnation point flow of a nanofluid toward an exponentially stretching sheet with nonuniform heat generation/absorption. *Journal of Thermodynamics*, **2013**, 764827 (2013)

[41] ABBASBANDY, S., HAYAT, T., ALSAEDI, A., and RASHIDI, M. M. Numerical and analytical solutions for Falkner-Skan flow of MHD Oldroyd-B fluid. *International Journal of Numerical Methods for Heat and Fluid Flow*, **24**, 390–401 (2014)

[42] TURKYILMAZOGLU, M. An effective approach for evaluation of the optimal convergence control parameter in the homotopy analysis method. *Filomat*, **30**, 1633–1650 (2016)

[43] AWAIS, M., SALEEM, S., HAYAT, T., and IRUM, S. Hydromagnetic couple-stress nanofluid flow over a moving convective wall: OHAM analysis. *Acta Astronautica*, **129**, 271–276 (2016)

[44] HAQ, R. U., HAMOUCH, Z., HUSSAIN, S. T., and MEKKAOUI, T. MHD mixed convection flow along a vertically heated sheet. *International Journal of Hydrogen Energy*, **42**, 15925–15932 (2017)

[45] HAYAT, T., AZIZ, A., MUHAMMAD, T., and ALSAEDI, A. Three-dimensional flow of Prandtl fluid with Cattaneo-Christov double diffusion. *Results in Physics*, **9**, 290–296 (2018)

[46] GHIASI, E. K. and SALEH, R. Unsteady shrinking embedded horizontal sheet subjected to inclined Lorentz force and Joule heating, an analytical solution. *Results in Physics*, **11**, 65–71 (2018)

[47] KUNNEGOWDA, T., MAHANTHESH, B., LORENZINI, G., and ANIMASAUN, I. L. Significance of induced magnetic field and exponential space dependent heat source on quadratic convective flow of Casson fluid in a micro-channel via HPM. *Mathematical Modelling of Engineering Problems*, **6**, 369–384 (2019)

[48] ULLAH, I., RAHIM, M. T., KHAN, H., and QAYYUM, M. Analysis of various semi-numerical schemes for magnetohydrodynamic (MHD) squeezing fluid flow in porous medium. *Propulsion and Power Research*, **8**, 69–78 (2019)

[49] HASSEN, W., KOLSI, L., MOHAMMED, H. A., GHACHEM, K., SHEIKHOLELAMI, M., and ALMESHAAL, M. A. Transient electrohydrodynamic convective flow and heat transfer of MWCNT-dielectric nanofluid in a heated enclosure. *Physics Letters A*, **384**, 126736 (2020)